Optics Letters

Quasi-monolithic heterodyne laser interferometer for inertial sensing

YANQI ZHANG[1,2] AND FELIPE GUZMAN[1,*]

[1] Texas A&M University, Aerospace Engineering & Physics, 701 H.R. Bright Bldg., College Station, Texas 77843, USA
[2] Wyant College of Optical Sciences, University of Arizona, 1630 E. University Blvd., Tucson, Arizona 85721, USA
*Corresponding author: felipe@tamu.edu

Received 17 August 2022; revised 1 September 2022; accepted 3 September 2022; posted 8 September 2022; published 27 September 2022

We present a compact heterodyne laser interferometer developed for high-sensitivity displacement sensing applications. This interferometer consists of customized prisms and wave plates assembled as a quasi-monolithic unit to realize a miniaturized system. The interferometer design adopts a common-mode rejection scheme to provide a high rejection ratio to common environmental noise. Experimental tests in vacuum show a displacement sensitivity level of 11 pm/$\sqrt{\text{Hz}}$ at 100 mHz and as low as 0.6 pm/$\sqrt{\text{Hz}}$ above 1 pm. The prototype unit is 20 mm × 20 mm × 10 mm in size and weighs 4.5 g, allowing subsequent integration in compact systems.

https://doi.org/10.1364/OL.473476

Introduction. Displacement measuring interferometry (DMI) has long been an integral part of precision manufacturing and metrology engineering. Recent advancements in optomechanics, such as monolithic optomechanical inertial sensors [1,2], extended the applications of DMI to the area of inertial sensing. Such optomechanical inertial sensors, operating at sub-hertz measurement bandwidths, consist of a mechanical resonator with a low resonant frequency of a few hertz to increase the thermal-limited acceleration sensitivity, and an optical readout system to perform dynamic measurements of the test mass displacement. The development of optical readout systems for low-frequency optomechanical inertial sensors faces several challenges. Firstly, the optical readout system is expected to achieve a high sensitivity in the millihertz frequency regime and simultaneously a large dynamic range to track the test mass motion. Owing to the low resonant frequency and, therefore, the low stiffness of the mechanical resonator, the test mass motion may reach amplitudes of several micrometers to a few millimeters when subjected to large accelerations. Secondly, the footprint of the optical readout system should be comparable to the size of the mechanical resonator to facilitate system integration. Various types of DMI technique exhibit a large dynamic range, but present other concerns at the same time. For example, deep phase modulation interferometry (DPMI) and deep frequency modulation interferometry (DFMI) [3] demonstrate displacement sensitivity of 20 pm/$\sqrt{\text{Hz}}$, but require complicated data processing algorithms for phase extraction. Furthermore, DFMI requires the use of lasers that are largely tunable in their frequency, which are typically complex, very expensive, and result in additional complications to the system regarding their operation and frequency stability. In this paper, we propose an interferometer design based on heterodyne interferometry, owing to its inherent directional sensitivity and fast response speed.

Efforts have been made to develop highly sensitive heterodyne displacement interferometers over the past decades using common-mode rejection schemes [4–8]. In the Laser Interferometer Space Antenna (LISA) [4] and its demonstration unit, LISA Pathfinder (LPF) [5,6], four heterodyne interferometers are integrated onto one bench as the optical readout system. This achieves a sensitivity level of 10 pm/$\sqrt{\text{Hz}}$ at 1 mHz on ground, and 30 fm/$\sqrt{\text{Hz}}$ in space when measuring the displacement of a free-falling test mass. However, the manufacture of this interferometer unit requires complicated alignment and bonding techniques, which makes it difficult to replicate and deploy in other sensing applications. Beyond space-based gravitational-wave observation, several other applications can benefit from such compact high-sensitivity laser interferometers, such as spacecraft drag-free control [9,10] or the characterization and calibration of laser direct writing lithography [11], which require precisions at or below the nanometer level, as well as dimensional metrology, and machining tools in manufacturing and precision measurements, striving precisions from picometers up to micrometers [12].

Other types of common-mode heterodyne interferometer [7,8] utilize a reference interferometer to monitor environmental noise and reach a picometer-level sensitivity at 100 mHz. However, the prototype systems have large footprints and require alignment of individual components, making them less appealing in portable applications.

To this end, and building on the expertise gained from the LPF interferometer development, we propose a novel configuration of a highly sensitive and compact optical assembly that comprises two heterodyne interferometers operating at normal incidence. On further development and benefiting from the design and operational principles of LPF, this results in a miniaturized quasi-monolithic unit with a high common-mode noise rejection. The proposed interferometer consists of a quasi-monolithic assembly of optical components, such as prisms and wave plates. The benchtop prototype achieves a displacement sensitivity level of 0.6 pm/$\sqrt{\text{Hz}}$ at 1 pm when tested in vacuum. The assembly

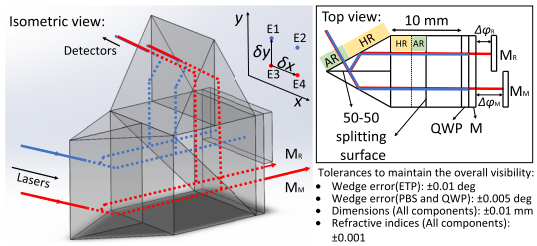

Fig. 1. Quasi-monolithic interferometer unit in isometric and top views. Two incoming laser beams are split into four beams by a 50–50 non-polarizing splitting surface embedded in a pair of ETPs. The beam pair with different frequencies forms one interferometer. Manufacturing tolerances for each component to maintain the overall interferometer visibility over 90% are listed in the figure.

unit fits in a 20 mm cube and weighs 4.5g, which makes it compatible with monolithically fabricated mechanical resonators [2] and highly compact instruments.

System design. The quasi-monolithic interferometer unit consists of two specially designed equilateral triangular prisms (ETPs), a polarizing beam splitter (PBS), a quarter wave plate (QWP), and a mirror (M), as depicted in Fig. 1. A 50–50 non-polarizing beam splitting surface is embedded in the middle of each ETP, dividing each ETP into two 30–60–90 prisms. The optical coatings on the side surfaces of the ETPs are split into two parts, where the part close to the 30° angle is treated with an anti-reflection (AR) coating and the other part has a high-reflectivity (HR) coating. Total internal reflection (TIR) is avoided in this assembly to maintain the polarization state of the incoming laser beams. The mirror M can be replaced by another HR coating to further reduce the system footprint.

After passing through two individual acousto-optical modulators (AOMs), two laser beams are shifted to slightly different frequencies and enter the side surface of the first ETP at normal incidence. These two beams are split into four after traversing the 50–50 splitting surface. All four beams are reflected by the HR coatings on the first ETP and enter the PBS perpendicularly. On the measurement end, the top two beams are reflected by the attached mirror M, which serves as the global reference. One of the bottom beams is reflected by a local reference mirror, M_R, which is fixed near the target, while the other bottom beam is incident on another mirror, M_M, which is mounted on the target. The reflected beams return to the PBS again and propagate toward the second ETP, where the beam pairs E_1 and E_3 and E_2 and E_4 overlap to build a reference interferometer (RIFO) and a measurement interferometer (MIFO), respectively, and are detected by their corresponding photodetectors (PDs).

The electric-field amplitudes of the four beams at the detection plane can be expressed as

$$E_1 = E_{10}\exp\left[i(\omega + \Delta\omega_1)t + \phi_0(0, \delta y)\right], \quad (1)$$

$$E_2 = E_{20}\exp\left[i(\omega + \Delta\omega_1)t + \phi_0(\delta x, \delta y)\right], \quad (2)$$

$$E_3 = E_{30}\exp\left[i(\omega + \Delta\omega_2)t + \phi_0(0, 0) + \Delta\phi_{\mathrm{R}}\right], \quad (3)$$

$$E_4 = E_{40}\exp\left[i(\omega + \Delta\omega_2)t + \phi_0(\delta x, 0) + \Delta\phi_{\mathrm{M}}\right], \quad (4)$$

where $\phi_0(x, y)$ represents the phase shift of each beam when propagating from the entry plane to the detection plane. The terms $\Delta\phi_{\mathrm{R}}$ and $\Delta\phi_{\mathrm{M}}$ denote the phase contributions from the optical path-length difference (OPD) between mirrors M and M_R and between mirrors M and M_M, respectively. The detected irradiance signals of the MIFO and the RIFO are expressed as

$$I_{\mathrm{M}} = I_{\mathrm{M0}}[1 - V_1\cos(\Delta\omega t + \phi_0(0, \delta y) + \Delta\phi_{\mathrm{M}})], \quad (5)$$

$$I_{\mathrm{R}} = I_{\mathrm{R0}}[1 - V_2\cos(\Delta\omega t + \phi_0(0, \delta y) + \Delta\phi_{\mathrm{R}})], \quad (6)$$

where V is the interferometer visibility, $\Delta\omega = \Delta\omega_2 - \Delta\omega_1$ is the heterodyne frequency, and $\phi_0(0, \delta y) = \phi_0(x, 0) - \phi_0(x, \delta y)$ is the phase difference between two vertically aligned beams due to any potential structural instability along the y direction. By performing the differential operation between the phase readouts from MIFO and RIFO, the y axis structural fluctuation terms $\phi_0(0, \delta y)$ cancel out, enhancing the overall system sensitivity. The target displacement d is calculated as

$$d = \frac{\Delta\phi}{2\cdot 2\pi}\lambda = \frac{\Delta\phi_{\mathrm{M}} - \Delta\phi_{\mathrm{R}}}{2\cdot 2\pi}\lambda, \quad (7)$$

where λ is the laser wavelength.

The spatially separated beams in the design mitigate inherent periodic errors in the heterodyne interferometer [13–15]. Owing to the compact size of the assembly, the optical paths between MIFO and RIFO are highly common, providing a high rejection ratio for common noise sources, such as temperature fluctuations. Manufacturing errors in the prisms, such as dimensions and wedge angles, can be compensated by adjusting the positions and incident angles of the input beams. We conducted a Monte Carlo analysis on the dimensions and geometry of the components to maintain the overall interferometer visibilities, V, above 90% at a 90% yield, and determine the tolerances (see Fig. 1) for the optical components. In this analysis, we considered fiber injectors with a limited resolution of 0.01 mm for the displacement and 0.01° as compensators for the angle of incidence.

Prototype characterization. We developed a prototype interferometer according to the design shown in Fig. 1, made of N-BK7 with coatings for a wavelength of 1550 nm. Individual components are cemented by UV curing using the adhesive NOA61 for index matching. The relative positions and orientations of two beam injectors can be easily adjusted during the alignment process with respect to the interferometer assembly, to maximize the visibility of the two interferometers. The prototype is tested inside a vacuum chamber that operates at 4 mPa. In this preliminary test, one static mirror serves as both the measurement and the reference mirror to characterize the interferometric system noise only. Figure 2 shows the logarithmic-averaged linear spectral density (LSD) of a 4-h measurement for the individual interferometers, MIFO and RIFO, and the differential displacement calculated using Eq. (7). The LSDs of the MIFO and RIFO measurements highly overlap, owing to the common paths between the two interferometers. The logarithmic-averaged traces shows that the MIFO and RIFO achieve a sensitivity level of $9.25\times -8\,\mathrm{m}/\sqrt{\mathrm{Hz}}$ at 100 mHz frequency, while the differential measurement enhances the sensitivity by over two orders of magnitude, reaching $1.16\times^{-11}$ $\mathrm{m}/\sqrt{\mathrm{Hz}}$ at 100 mHz.

We investigated various noise sources, including temperature fluctuations, nonlinear OPD noise, laser frequency noise, pressure fluctuations, and detection system noise, to estimate their contribution to the displacement measurement, as shown in the dashed lines in Fig. 2.

Two thermistors are used as temperature sensors. One of them is installed inside the vacuum chamber, attached to the breadboard, and the other one is outside the chamber, in air, to measure

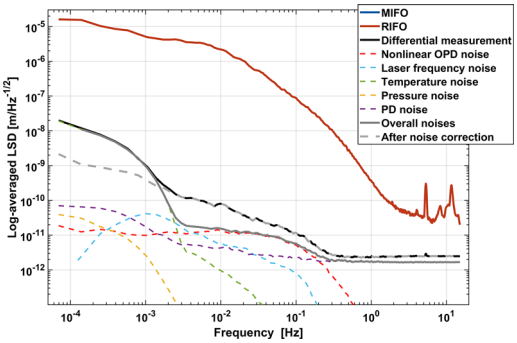

Fig. 2. Logarithmic-averaged LSDs of 4-h measurements from individual interferometers, MIFO and RIFO, and differential measurement, as well as contributions from different noise sources. The sensitivity levels of the individual interferometers are both $9.25 \times^{-8}$ m/$\sqrt{\text{Hz}}$ at 100 mHz; the overall systematic sensitivity is enhanced to $1.16 \times^{-11}$ m/$\sqrt{\text{Hz}}$ at 100 mHz by the differential operation.

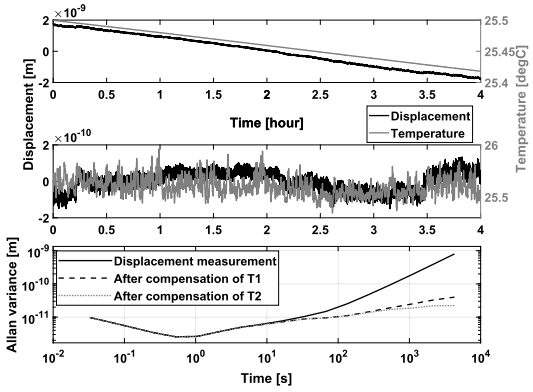

Fig. 3. (a) Original displacement measurement and temperature measurement T_1 with temperature sensor installed inside chamber; (b) displacement after compensating thermal drift using T_1, and temperature measurement T_2 with temperature sensor installed outside chamber; (c) Allan variances of original displacement measurement, and displacement after compensating for T_1 and T_2 measurements, respectively.

temperature fluctuations at a sampling frequency of 1 pm. Figure 3(a) shows the time series of the 4-h measurements of the differential displacement and the temperature measurement (T_1) inside the chamber. The displacement measurement is corrected for the thermal drift using the T_1 measurement, resulting in the trace shown in Fig. 3(b), along with the temperature measurement (T_2) outside the chamber. Figure 3(c) shows the Allan deviation of the differential displacement to be $1.8 \times^{-11}$ m over an integration time of 1000 s after correction. The temperature coupling coefficients for T_1 and T_2 are estimated to be $4.41 \times^{-8}$ m/K and $6.64 \times^{-10}$ m/K.

The electromagnetic interference of the radio-frequency (RF) signals that drive the two AOMs imprints spurious sidebands onto the laser beams, resulting in a ghost signal with the same heterodyne frequency f_{het}. The phase error introduced by this parasitic signal is referred to as the nonlinear OPD noise, the amplitude of which is related to the phase readouts of the individual interferometers $\Delta\phi_{\text{M}}$ and $\Delta\phi_{\text{R}}$. By applying a linear fitting algorithm [8], we can separate this noise contribution from the

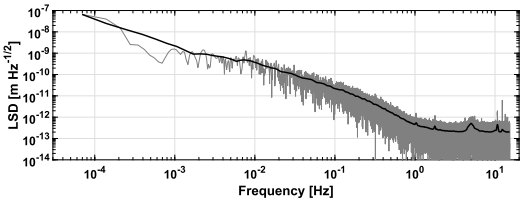

Fig. 4. LSD of 4-h differential measurement with improved PD system performance. The sensitivity floor of this differential measurement is 0.6 pm/$\sqrt{\text{Hz}}$ above 1 pm.

displacement measurement. In the experimental setup, this noise effect is mitigated by RF shielding.

The OPD between the two interferometer arms determines the coupling coefficient of the laser frequency noise. The proposed quasi-monolithic interferometer is designed to have a symmetric configuration that helps mitigate the effects of laser frequency noise. Moreover, in the test setup where only one static mirror is used for both measurement and reference mirrors, the OPD is further reduced between the two individual interferometers. In the test setup, the laser frequency noise is monitored using a self-referenced fiber delay-line interferometer (DIFO) [8] that amplifies the laser frequency noise effects using intentionally unequal arm lengths. The laser frequency noise is extracted from the phase measurement of the DIFO, which is bandpass filtered between 1 mHz and 100 mHz to mitigate the contributions of other noise sources [8].

We recorded the displacement measurements when the vacuum pumps were turned off to prevent mechanical vibrations from coupling into the phase measurement. In this case, the pressure inevitably rises inside the chamber and is monitored by a pressure gauge at a sampling frequency of 1 pm. The coupling coefficient of the pressure variation is estimated to be $2.1 \times^{-12}$ m/Pa, based on a measurement of the pump-down process.

Detection system noise, such as analog-to-digital conversion (ADC), photodetector [16], and phasemeter [17] noise, determines the lowest noise floor that an interferometric system can achieve. A zero-test is performed for both PDs, where the detected irradiance signal from a single PD is split into two input channels of the phasemeter.

In the low-frequency regime below 1 mHz, temperature fluctuations are the dominant noise sources. In the frequency bandwidth above 1 pm, the interferometer performance is limited by the PD noise, which can be further improved by increasing the optical power incident on the photodetectors, as well as by improving the interferometer alignment for a better fringe contrast. We took another 4-h measurement with these improvements under the same environmental conditions, as shown in Fig. 4. This plot shows that, for the differential measurement, the LSD is $6 \times^{-13}$ m/$\sqrt{\text{Hz}}$ at 1 pm.

Laser frequency noise and temperature fluctuations are likely to be the main factors limiting the interferometer sensitivity at low frequencies, because we are operating a free-running laser and our fiber-based DIFO is not a good sensor of laser frequency fluctuations over this bandwidth. Furthermore, when using a free-running laser, this is likely to become a significant noise source when the axial distance between the reference mirror M_R and the measurement mirror M_M increases. This can be mitigated by adopting laser frequency stabilization systems with active feedback control. Since the test mirrors, the optical assembly,

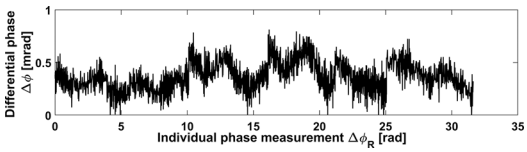

Fig. 5. Differential phase readout $\Delta\phi$ with respect to one of the individual phase readouts, $\Delta\phi_{\mathrm{R}}$.

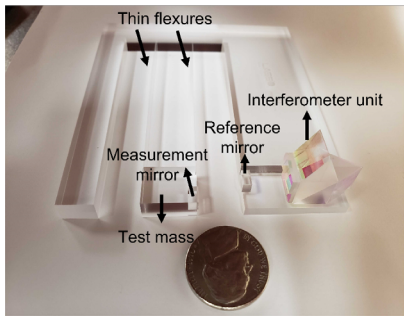

Fig. 6. System assembly, integrating proposed quasi-monolithic interferometer as optical readout system with monolithically fabricated fused-silica mechanical resonator [2], to construct portable and highly sensitive optomechanical inertial sensor. The overall footprint is compared with a US nickel in the picture.

and the fiber injectors are all currently supported with off-the-shelf kinematic mounts, we consider it plausible that the residual noise floor and its rise toward lower frequencies originate in their inherent mechanical and material instabilities [18].

We have designed this interferometer assembly to mitigate inherent periodic errors. Any stray light originating at the optical interfaces due to normal incidence would typically result in a periodic error pattern in the interferometer signal that can be easily recognized by plotting the differential phase between the two interferometers with respect to a single interferometer phase [19]. Figure 5 shows the differential phase $\Delta\phi$ versus one of the individual phase readouts, $\Delta\phi_{\mathrm{R}}$, over a few interferometer fringes (10 rad). It can be clearly observed that no consistent periodic pattern is recognizable in this plot, where we conclude that any effect from potential stray light is negligible.

Figure 6 shows the system assembly where the interferometer unit is integrated as the optical readout system for an optomechanical inertial sensor. A notch is etched on the test mass of the mechanical resonator to mount the mirror M_M. The mirror M_R is mounted on the baseplate of the resonator. The overall footprint of the inertial sensor is $90\,\mathrm{mm} \times 80\,\mathrm{mm} \times 20\,\mathrm{mm}$, providing a compact solution to highly sensitive accelerometers.

Summary and outlook. In this paper, we present the design of a quasi-monolithic heterodyne laser interferometer assembly that utilizes a common-mode rejection scheme to enhance the overall sensitivity while maintaining a very compact form factor. Preliminary tests in our laboratory show a sensitivity level of $0.6\,\mathrm{pm}/\sqrt{\mathrm{Hz}}$ above 1 pm in vacuum, which is greatly enhanced from two individual heterodyne interferometers.

On integration of the interferometer unit with the mechanical resonator, upcoming work will involve true acceleration measurements at low frequencies using the fully assembled optomechanical inertial sensing units. Such a unit will also include improvements, such as laser frequency stabilization using a fiber-coupled HCN gas cell and lower-noise photoreceivers. Such a laser frequency stabilization system is under development in our laboratory, utilizing the HCN gas cell to establish the molecular spectroscopy locking of the laser frequency.

Funding. National Aeronautics and Space Administration (80NSSC 20K1723); National Science Foundation (ECCS-1945832, PHY-2045579); National Geospatial-Intelligence Agency (HMA04762010016).

Acknowledgments. We thank Adam Hines, Bo Stoddart, and Lee Ann Capistran for implementing the data acquisition script for temperature and pressure measurements. We also thank Dr. Jose Sanjuan for proofreading the manuscript.

Disclosures. The authors declare no conflicts of interest.

Data availability. Data underlying the results presented in this paper are not publicly available but may be obtained from the authors upon reasonable request.

REFERENCES

1. F. Guzman, L. M. Kumanchik, J. M. Taylor, and J. R. Pratt, "Optomechanical gravimeter," U.S. patent application 10,545,259B2 (28January2020).
2. A. Hines, L. Richardson, H. Wisniewski, and F. Guzman, Appl. Opt. **59**, G167 (2020).
3. G. Heinzel, F. G. Cervantes, A. F. G. Marín, J. Kullmann, W. Feng, and K. Danzmann, Opt. Express **18**, 19076 (2010).
4. G. Heinzel, V. Wand, A. García, O. Jennrich, C. Braxmaier, D. Robertson, K. Middleton, D. Hoyland, A. Rüdiger, R. Schilling, U. Johann, and K. Danzmann, Class. Quantum Grav. **21**, S581 (2004).
5. V. Wand, F. Guzmán, G. Heinzel, and K. Danzmann, in *Laser Interferometer Space Antenna: 6th International LISA Symposium*, Vol. 873 of *American Institute of Physics Conference Series*, S. M. Merkovitz and J. C. Livas, eds. (2006), pp. 689–696.
6. F. Guzman, "Gravitational wave observation from space: optical measurement techniques for lisa and lisa pathfinder," Ph.D. thesis (Max Planck Institute for Gravitational Physics & Gottfried Wilhelm Leibniz Universität Hannover, Hannover, Germany, 2009).
7. K.-N. Joo, E. Clark, Y. Zhang, J. D. Ellis, and F. Guzmán, J. Opt. Soc. Am. A **37**, B11 (2020).
8. Y. Zhang, A. Hines, G. Valdes, and F. Guzman, Sensors **21**, 5788 (2021).
9. M. S. Guilherme, W. C. Leite Filho, and S. Theil, Aerosp. Sci. Technol. **12**, 365 (2008).
10. R. De Rosa, L. Di Fiore, F. Garufi, A. Grado, A. La Rana, and L. Milano, Astroparticle Phys. **34**, 394 (2011).
11. J. Jaramillo, A. Zarzycki, J. Galeano, and P. Sandoz, Sensors **17**, 278 (2017).
12. H. Hansen, K. Carneiro, H. Haitjema, and L. De Chiffre, CIRP Ann. **55**, 721 (2006).
13. C.-M. Wu and R. Deslattes, Appl. Opt. **37**, 6696 (1998).
14. K.-N. Joo, J. D. Ellis, E. S. Buice, J. W. Spronck, and R. H. M. Schmidt, Opt. Express **18**, 1159 (2010).
15. J. D. Ellis, A. J. H. Meskers, J. W. Spronck, and R. H. M. Schmidt, Opt. Lett. **36**, 3584 (2011).
16. F. G. Cervantes, J. Livas, R. Silverberg, E. Buchanan, and R. Stebbins, Class. Quantum Grav. **28**, 094010 (2011).
17. O. Gerberding, C. Diekmann, J. Kullmann, M. Tröbs, I. Bykov, S. Barke, N. C. Brause, J. J. Esteban Delgado, T. S. Schwarze, J. Reiche, K. Danzmann, T. Rasmussen, T. V. Hansen, A. Enggaard, S. M. Pedersen, O. Jennrich, M. Suess, Z. Sodnik, and G. Heinzel, Rev. Sci. Instrum. **86**, 074501 (2015).
18. J. D. Ellis, "Optical metrology techniques for dimensional stability measurements," Ph.D. thesis (Delft University of Technology, Delft, Netherlands, 2010).
19. V. Wand, J. Bogenstahl, C. Braxmaier, K. Danzmann, A. García, F. Guzmán, G. Heinzel, J. Hough, O. Jennrich, C. Killow, D. Robertson, Z. Sodnik, F. Steier, and H. Ward, Class. Quantum Grav. **23**, S159 (2006).